Asian Journal of Chemistry; Vol. 37, No. 12 (2025), 3011-3018
ASIAN JOURNAL OF CHEMISTRY
https://doi.org/10.14233/ajchem.2025.34638

Solvothermal Synthesis of Flower-like CMTS Nanostructures for High-Efficiency Photocatalytic Degradation of Organic Dyes Under Natural Sunlight

SARATHKUMAR ANBUSELVAN, NITHISHKUMAR SRINIVASAN and SIVAKUMAR GANESAN*

Department of Physics, Annamalai University, Annamalai Nagar-608002, India

*Corresponding author: E-mail: gsk.csil@gmail.com

Received: 5 August 2025 *Accepted*: 30 September 2025 *Published online*: 30 November 2025 AJC-22189

In this study, Cu_2MnSnS_4 (CMTS) nanoparticles with a flower-like nanostructure were successfully synthesized *via* a solvothermal method by varying the reaction durations to investigate their structural, morphological and photocatalytic properties. X-ray diffraction (XRD) and Raman spectroscopy confirmed the formation of a single-phase kesterite structure at prolonged reaction time (24 h), while shorter durations resulted in mixed phases. SEM analysis revealed the evolution of well-defined flower-like architectures composed of ultrathin nanosheets in the 24 h sample, which exhibited improved crystallinity and phase purity. XPS analysis confirmed the presence of Cu^{+}, Mn^{2+}, Sn^{4+} and S^{2-} oxidation states. The optical characterization using UV-Vis diffuse reflectance spectroscopy revealed strong visible light absorption with a narrowed bandgap of 1.66 eV for the 24 h sample. The photocatalytic activity of CMTS nanoparticles was evaluated under natural sunlight for the degradation of methylene blue (MB) and crystal violet (CV) dyes. The Cu_2MnSnS_4-24 ($CMTS_{24}$) catalyst demonstrated superior degradation efficiencies of 76% for MB and 73% for CV within 50 min, attributed to its high surface area, improved charge carrier separation and enhanced light-harvesting capability. These findings highlight the crucial role of reaction time in determining the structural and functional properties of CMTS nanomaterials, establishing $CMTS_{24}$ as a promising candidate for solar-driven photocatalytic wastewater treatment applications.

Keywords: Copper manganese tin sulfide (CMTS), Solvothermal synthesis, Nano-flower, Photocatalytic activity.

INTRODUCTION

The increasing discharge of synthetic dyes into aquatic ecosystems has become a critical environmental concern, primarily due to their persistent, non-biodegradable nature [1]. Industrial sectors such as textiles, leather and paper extensively use organic dyes like methylene blue (MB) and crystal violet (CV), which are commonly detected in wastewater effluents. These dyes not only cause severe water colouration but also pose significant threats to aquatic life and human health due to their carcinogenic and mutagenic properties [2,3].

Conventional wastewater treatment techniques such as biological, physical and chemical methods often prove inadequate in completely eliminating these recalcitrant dyes [4,5]. As a result, the development of cost-effective and sustainable technologies for their efficient degradation remains an urgent need. Among various advanced oxidation processes, semiconductor-based photocatalysis has emerged as a promising green technology for wastewater remediation. This approach utilizes solar energy to generate electron–hole pairs, which drive redox reactions that ultimately mineralize toxic organic compounds into harmless products like CO_2 and H_2O [6,7].

In recent years, growing research has focused on designing advanced visible-light-responsive photocatalysts that function efficiently under natural sunlight [8]. Among various semiconducting materials, quaternary metal chalcogenides such as Cu_2ZnSnS_4 (CZTS), Cu_2NiSnS_4 (CNTS) and Cu_2CoSnS_4 (CCTS) have gained attention due to their optimal bandgap energies, strong visible light absorption, abundance of constituent elements and non-toxic nature [9]. Within this class, Cu_2MnSnS_4 (CMTS) has recently emerged as a promising candidate owing to its suitable bandgap, high absorption coefficient and environmentally benign composition [10,11]. While kesterite-phase chalcogenides have been extensively investigated for photovoltaic and thermoelectric applications, their potential for photocatalytic degradation of organic pollutants under natural sunlight remains relatively underexplored. Achieving phase-pure CMTS nanoparticles with controlled

morphology and high crystallinity is essential to enhance their photocatalytic efficiency.

The solvothermal method offers several advantages for synthesizing high-quality CMTS nanostructures, including simplicity, scalability and excellent control over morphology and particle size. However, systematic studies on solvothermally synthesized CMTS, particularly for the simultaneous degradation of multiple dyes and the role of tailored morphology on photocatalytic performance, are still scarce. Therefore, the present study aims to fill this gap by synthesizing phase-pure Cu_2MnSnS_4 nanoparticles using a straightforward solvothermal approach, followed by detailed structural and morphological characterization. Furthermore, their photocatalytic efficiency is evaluated through the degradation of methylene blue and crystal violet dyes under natural sunlight. The outcomes of this work are expected to contribute toward the development of efficient, low-cost and eco-friendly photocatalysts for the wastewater treatment.

EXPERIMENTAL

Copper(II) chloride dihydrate ($CuCl_2·2H_2O$, ≥ 99.5%), manganese(II) chloride dihydrate ($MnCl_2·2H_2O$, ≥ 98.0%) and tin(II) chloride dihydrate ($SnCl_2·2H_2O$, ≥ 99.5%) were selected as the respective metal sources, while thiourea (CH_4N_2S, ≥ 99.5%) was used as sulphur donor. Ethylene glycol served as solvent due to its high boiling point and stabilizing prop-erties. All reagents were of analytical grade and purchased from Sigma-Aldrich, USA without further purification.

Synthesis of CMTS: Single-phase Cu_2MnSnS_4 (CMTS) nanoparticles were synthesized *via* a solvothermal route using high-purity precursors. A homogeneous solution was prepared by dissolving 0.06 M $CuCl_2·2H_2O$, 0.03 M $MnCl_2·2H_2O$, 0.03 M $SnCl_2·2H_2O$ and 0.12 M CH_4N_2S in 40 mL of ethylene glycol. The mixture was magnetically stirred for 45 min to ensure complete dissolution and uniform mixing of the reactants. The resulting solution was then transferred into a 100 mL Teflon-lined stainless steel autoclave and heated at 210 ºC for two different durations *viz*. 12 h and 24 h to study the effect of reaction time on the phase formation and morphological features of the synthesized CMTS nanoparticles. Upon com-pletion of the solvothermal process, the autoclave was allowed to cool naturally to room temperature. The precipitates were collected by vacuum filtration using Whatman filter paper, followed by repeated washing with ethanol to remove any un-reacted precursors and residual organic content. The obtained solid product was then dried in a hot air oven at 80 ºC for 3 h to ensure complete removal of moisture.

Photocatalytic activity: The photocatalytic activity of CMTS nanoparticles was evaluated by monitoring the degradation of methylene blue (MB) and crystal violet (CV) dyes under natural sunlight. Aqueous dye solutions were prepared with concentrations of 10^{-4} M (MB) and 10^{-5} M (CV) by dissolving the dyes in 1 L of distilled water. For each test, 100 mL of dye solution was mixed with 10 mg of CMTS catalyst in a 250 mL beaker and the mixture was continuously stirred using a magnetic stirrer. The experiments were carried out under direct sunlight between 11:00 a.m. and 2:00 p.m. on cloud-free days to ensure stable irradiation conditions. At regular intervals of 10 min, aliquots were withdrawn and analyzed using a UV-visible spectrophotometer to track the degradation progress. Photocatalytic degradation efficiency (η%) was calculated using eqn. 1 [12]:

$$\text{Efficiency } (\eta\%) = \left(1 - \frac{C}{C_o}\right) \times 100$$

where C_o and C represent the initial and residual concentrations (absorbance) of the dye, respectively.

Characterization techniques: The CMTS samples synthesized at 12 h ($CMTS_{12}$) and 24 h ($CMTS_{24}$) were thoroughly characterized. The phase identification and crystallinity were analyzed using powder X-ray diffraction (X'Pert PRO, PANalytical, Germany) with Cu*K*α radiation (λ = 1.54060 Å) at 40 kV and 30 mA. Raman spectroscopy (Seiki, Japan) was used to confirm the vibrational features. Surface morphology was observed by SEM (JEOL JSM-IT200) and elemental composition was examined using EDS. XPS analysis (PHI Versaprobe) provided information on elemental states and surface chemistry. The optical bandgap was determined using UV-Vis diffuse reflectance spectroscopy (Shimadzu RF-6000) and the photocatalytic efficiency was tested with a Shimadzu UV-1800 UV-Vis spectrophotometer.

RESULTS AND DISCUSSION

XRD analysis: The crystallographic structure of the CMTS nanoparticles synthesized at different reaction durations was examined using X-ray diffraction (XRD) and the resulting patterns are depicted in Fig. 1. For the sample synthesized at 12 h ($CMTS_{12}$) (Fig. 1a), diffraction peaks were observed at 2θ values of 28.42º, 47.89º and 55.68º, corresponding to the (112), (204) and (312) planes of a tetragonal structure. Additional peaks at 32.29º and 58.97º, indexed to the (200) and (224) planes, suggest the presence of a mixed-phase composition comprising Cu_2MnSnS_4 and Cu_2SnS_3, in agreement with the JCPDS card No. 89-4714 [13].

To obtain a pure phase of Cu_2MnSnS_4, the reaction time was extended to 24 h ($CMTS_{24}$) (Fig. 1b). The XRD pattern exhibited distinct and sharp peaks at 2θ = 28.41º, 47.43º and 55.51º, which correspond to the (112), (204) and (312) planes of a kesterite-type tetragonal structure. These reflections matched well with JCPDS card No. 89-1952, confirming the formation of a single phase ($CMTS_{24}$) without any secondary phases [14]. The $CMTS_{24}$ sample showed more intense and narrower diffraction peaks compared to the $CMTS_{12}$ sample, indicating improved crystallinity and phase purity. The absence of any additional peaks confirmed the successful formation of a pure CMTS phase. To estimate the average crystallite size, the Debye-Scherrer equation was employed using eqn. 2:

$$D = \frac{K\lambda}{\beta \cos\theta} \quad (2)$$

where D is the crystallite size, k is the shape factor; λ is the X-ray wavelength; β is the full width at half maximum (FWHM) and θ is the Bragg angle [15]. The synthesized $CMTS_{12}$ sample exhibited an average crystallite size of approximately 25

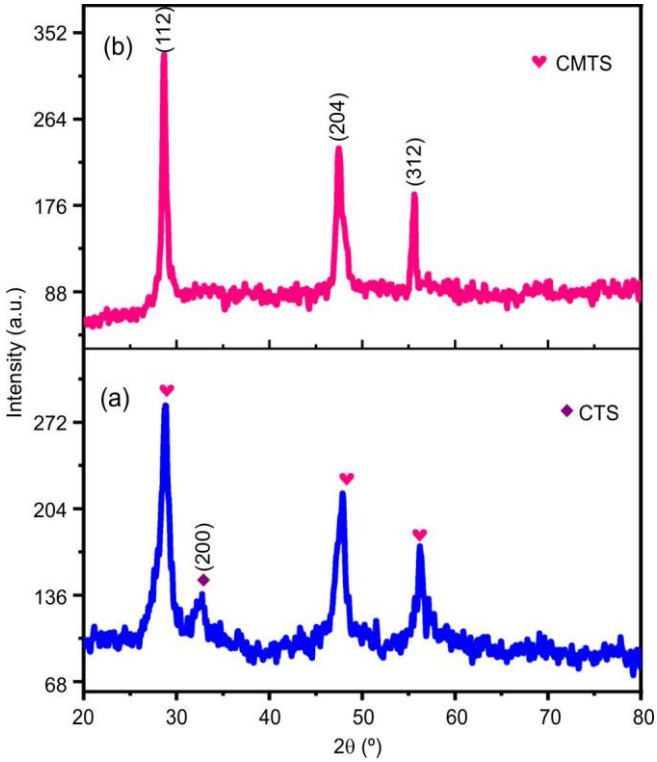

Fig. 1. XRD patterns of Cu_2MnSnS_4 nanoparticles synthesized at different reaction durations at (a) 12 h and (b) 24 h

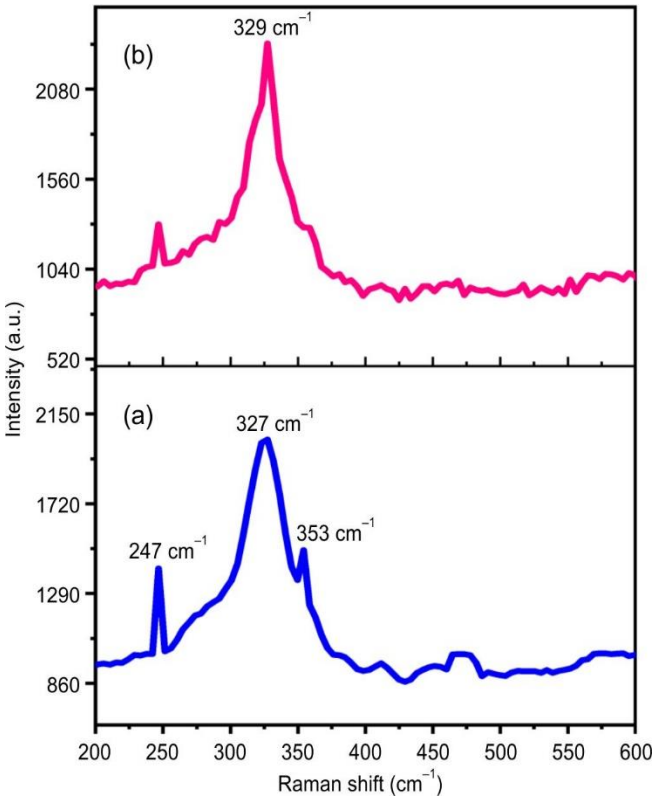

Fig. 2. Raman spectra of Cu_2MnSnS_4 nanoparticles at different reaction durations at (a) 12 h and (b) 24 h

nm, while the $CMTS_{24}$ sample showed a slightly reduced size of about 22 nm, indicating improved crystallinity and more defined structural features. This structural refinement underscores the critical role of reaction time in influencing phase formation and crystal quality [16].

Raman spectral analysis: Raman spectroscopy was employed to further investigate the structural evolution and phase composition of CMTS nanoparticles synthesized at different reaction times, as illustrated in Fig. 2a-b. In case of $CMTS_{12}$ sample (Fig. 2a), distinct peaks were observed at 247 cm^{-1}, 327 cm^{-1} and 353 cm^{-1}. These vibrational modes suggest the coexistence of both Cu_2MnSnS_4 (CMTS) and Cu_2SnS_3 phases, indicating an incomplete phase transformation at shorter reaction duration [14,17].

For $CMTS_{24}$ sample, significant changes were observed in the Raman profile. As shown in Fig. 2b, a stronger and sharper peak appears at 329 cm^{-1}, which corresponds to the characteristic A-mode vibration of the sulphur sublattice in the kesterite CMTS structure [18]. Moreover, a shoulder peak at 247 cm^{-1} further supports the presence of the CMTS phase. Importantly, the disappearance of the 353 cm^{-1} peak typically associated with the Cu_2SnS_3 secondary phase confirms the successful formation of a pure CMTS phase after prolonged reaction time. These spectral features strongly correlate with the XRD results, reinforcing the conclusion that extending the synthesis time to 24 h facilitates the development of a single-phase, crystalline CMTS material with enhanced structural integrity.

Surface morphology and elemental composition: Fig. 3a-b display SEM images of $CMTS_{12}$ sample at lower (10,000×) and higher (30,000×) magnifications, respectively. The lower magnification image (Fig. 3a) reveals agglomerated particle

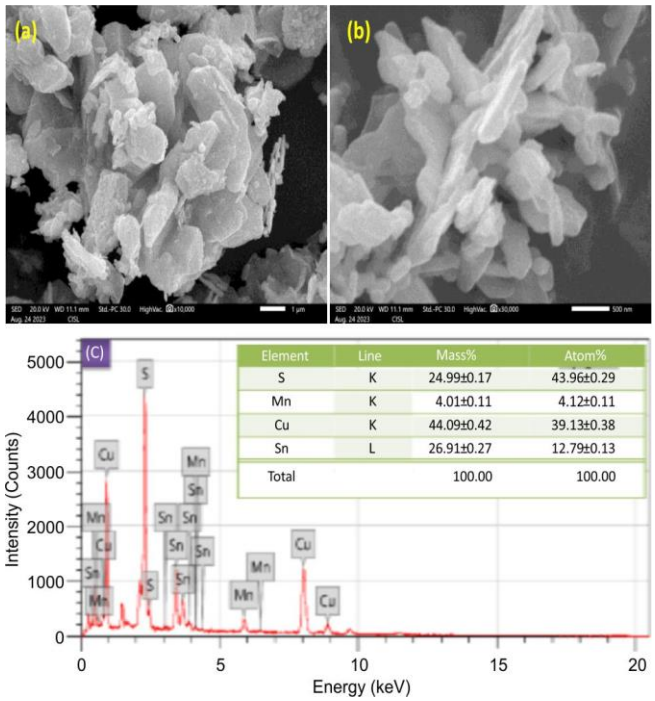

Fig. 3a-c. SEM image and EDS spectrum of the $CMTS_{12}$ sample

structures with an average size of approximately 1 μm. At higher magnification (Fig. 3b), the particles exhibit a partially flower-like morphology composed of loosely arranged nanosheets [10]. These sheets show lateral spreading and thin, layered textures, with individual sheet thickness estimated to be less than 30 nm.

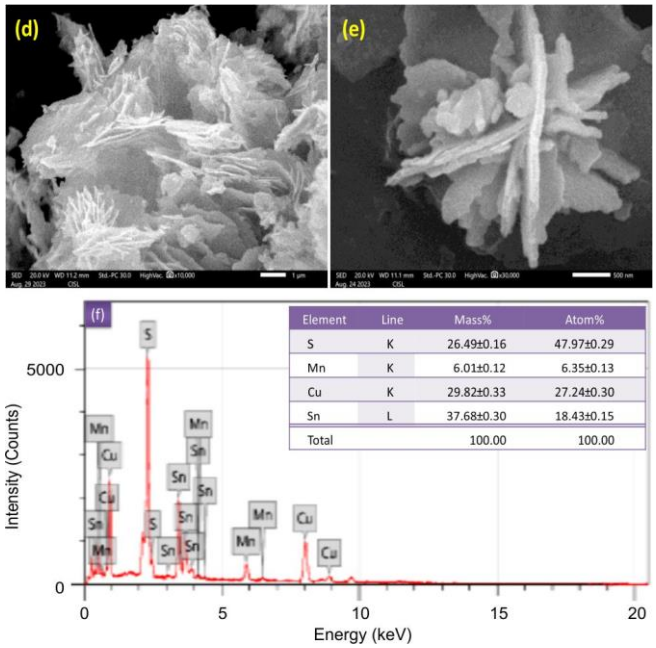

Fig. 3d-f. SEM image and EDS spectrum of the $CMTS_{24}$ sample

Fig. 3d-e present SEM images of $CMTS_{24}$ sample, also captured at (10,000×) and (30,000×) magnifications, respectively. Compared to $CMTS_{12}$ sample, the morphology is more developed, with flower-like assemblies more clearly defined. The structures observed at low magnification (Fig. 3d) have an average diameter of around 1 μm. High magnification images (Fig. 3e) reveal that the flower-like shapes are made of tightly packed, intergrown nanosheets with improved structural order [19]. The thickness of these sheets is again estimated to be below 25 nm.

The EDS analysis results for both $CMTS_{12}$ and $CMTS_{24}$ solvothermally synthesized samples are presented in Figs. 3c and 3f, respectively. For $CMTS_{12}$ sample, the atomic composition reveals the successful incorporation of S (43.96 ± 0.29 at.%), Cu (39.13 ± 0.38 at.%), Sn (12.79 ± 0.13 at.%) and Mn (4.12 ± 0.11 at.%) without any detectable impurities. Copper constitutes the primary metallic species, followed by tin and a minor amount of manganese. The elevated sulphur content suggests effective sulfidation and supports the formation of a stoichiometrically balanced Cu-rich quaternary metal sulphide. The homogeneity of the elemental distribution indicates that the sample exhibits good chemical uniformity. Fig. 3f in contrast, the $CMTS_{24}$ sample exhibits a modified elemental composition, with S (47.97 ± 0.29 at.%) being the most abundant, followed by Cu (27.24 ± 0.30 at.%), Sn (18.43 ± 0.15 at.%) and Mn (6.35 ± 0.13 at.%). The increased Sn and Mn contents and decreased Cu proportion relative to the $CMTS_{12}$ sample suggest time-dependent compositional tuning during the extended solvothermal reaction. This variation in elemental ratios indicates a shift toward a more Sn- and Mn-rich sulphide phase, likely contributing to the growth of more defined and structurally evolved nanostructures [20].

The overall improvement in uniformity and compactness of the nanostructures after 24 h ($CMTS_{24}$) indicates enhanced the particle growth and self-assembly due to the extended reaction time under solvothermal conditions. The $CMTS_{24}$ sample, with its well-defined sheet-like morphology and compact flower-like architecture, is considered optimal based on XRD, Raman and FESEM analyses. Such hierarchical nanosheet structures are expected to offer enhanced surface area and active sites, making them suitable candidates for photocatalytic applications.

Optical properties: The optical absorption characteristics of CMTS nanoparticles synthesized at different solvothermal reaction times (12 h and 24 h) were evaluated using UV-Vis diffuse reflectance spectroscopy (UV-DRS) in the wavelength range of 200-800 nm (Fig. 4a). Both samples exhibited strong absorption in the visible region, which is beneficial for photocatalytic applications under solar irradiation [21]. To estimate the optical bandgap energy (E_g), the Tauc plot method was applied based on the equation:

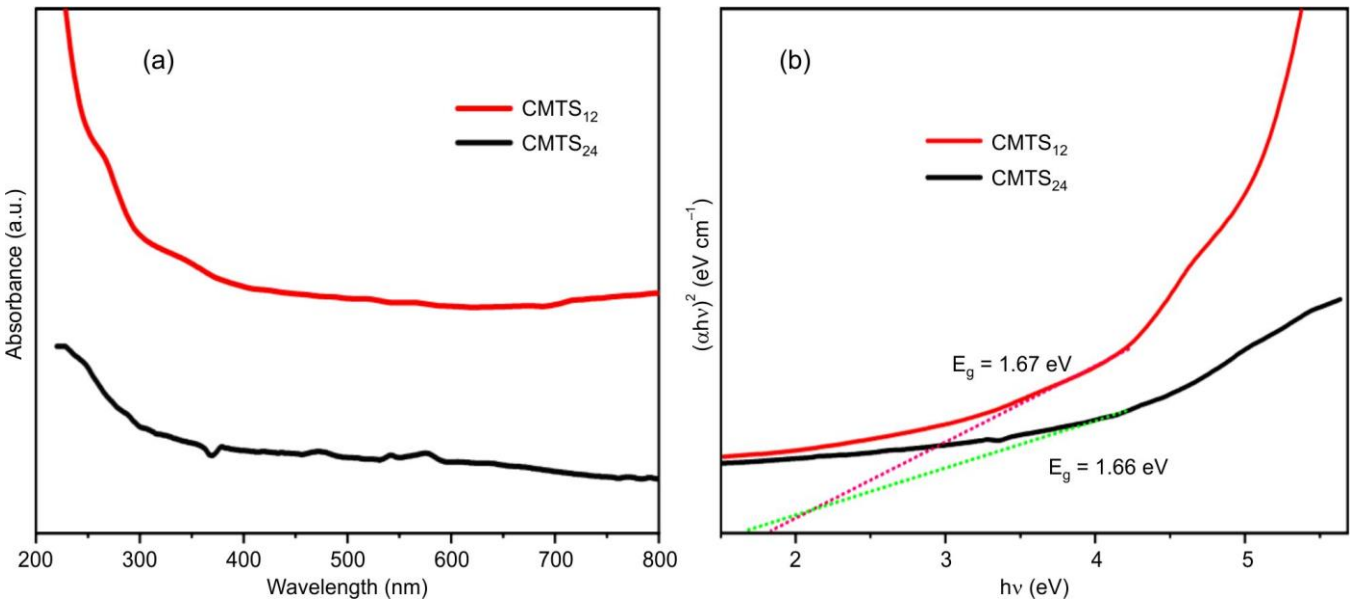

Fig. 4. (a) UV-DRS absorbance spectra of $CMTS_{12}$, $CMTS_{24}$ and (b) optical bandgap of $CMTS_{12}$, $CMTS_{24}$

$$\alpha h\nu = A(h\nu - E_g)^n \quad (3)$$

where α is the absorption coefficient, $h\nu$ represents the photon energy, E_g is the bandgap energy and A is a constant. For direct bandgap semiconductors, the value of n is taken as ½. The bandgap energies were derived by extrapolating the linear portion of the Tauc plots (Fig. 4b) onto the energy axis. The bandgap values for the $CMTS_{12}$ and $CMTS_{24}$ samples were found to be approximately 1.67 eV and 1.66 eV, respectively. The slight reduction in bandgap with increased reaction time enhances the absorption of lower-energy visible light, thereby improving the efficiency of photocatalytic processes [22].

These results highlight that tailoring the reaction time effectively tunes the optical response of CMTS nanomaterials, thereby enhancing their potential for sun-light-driven photocatalytic dye degradation. The XRD and Raman analyses further confirmed that the $CMTS_{24}$ sample attained optimized structural and phase purity, making it suitable for advanced photocatalytic investigations.

X-ray photoelectron spectroscopy (XPS): The chemical states and elemental composition of the $CMTS_{24}$ sample were examined using X-ray photoelectron spectroscopy (XPS). Fig. 5a-d presents the XPS spectra for Cu 2p, Mn 2p, Sn 3d and S 2p. The Cu 2p spectrum revealed two peaks at binding energies of 931 eV ($2p_{3/2}$) and 951.2 eV ($2p_{1/2}$), separated by 19.8 eV, which confirms the presence of Cu^+ oxidation state [23]. For Mn, the 2p spectrum displayed peaks at 641.9 eV and 653.6 eV, corresponding to Mn $2p_{3/2}$ and Mn $2p_{1/2}$, respectively, with a binding energy separation of 11.7 eV, signifying the Mn^{2+} oxidation state [24]. The Sn 3d spectrum showed a doublet at 485.3 eV ($3d_{5/2}$) and 494 eV ($3d_{3/2}$), with an energy difference of 8.7 eV, confirming the presence of Sn^{4+} [16]. The S 2p spectrum exhibited peaks at 160.77 eV (S $2p_{3/2}$) and 162.00 eV (S $2p_{1/2}$), with an additional peak at 168.36 eV, indicating the presence of sulphur in a higher oxidation state, which further validates the S^{2-} oxidation state. This comprehensive XPS analysis reveals that the CMTS material contains Cu^+, Mn^{2+}, Sn^{4+} and S^{2-} oxidation states, consistent with the expected chemical composition for Cu_2MnSnS_4 [25]. The consistency between the EDX and XPS results, along with the absence of impurity peaks, further affirms the high purity and correct stoichiometry of the synthesized material, indicating its suitability for the intended applications.

Photocatalytic activity: The photocatalytic degradation behaviour of methylene blue (MB) and crystal violet (CV) dyes under natural sunlight irradiation was systematically examined using $CMTS_{24}$ nanoparticles. The degradation efficiency was monitored through UV-Vis spectrophotometry, as depicted in Fig. 6a-b, presents the distinct absorption peaks of MB at 663 nm and CV at 570 nm in their respective blank dye solutions [26]. Upon the addition of 0.05 g of $CMTS_{24}$ catalyst, a progressive decline in absorbance was observed with increasing irradiation time, indicating effective photodegradation of both dyes.

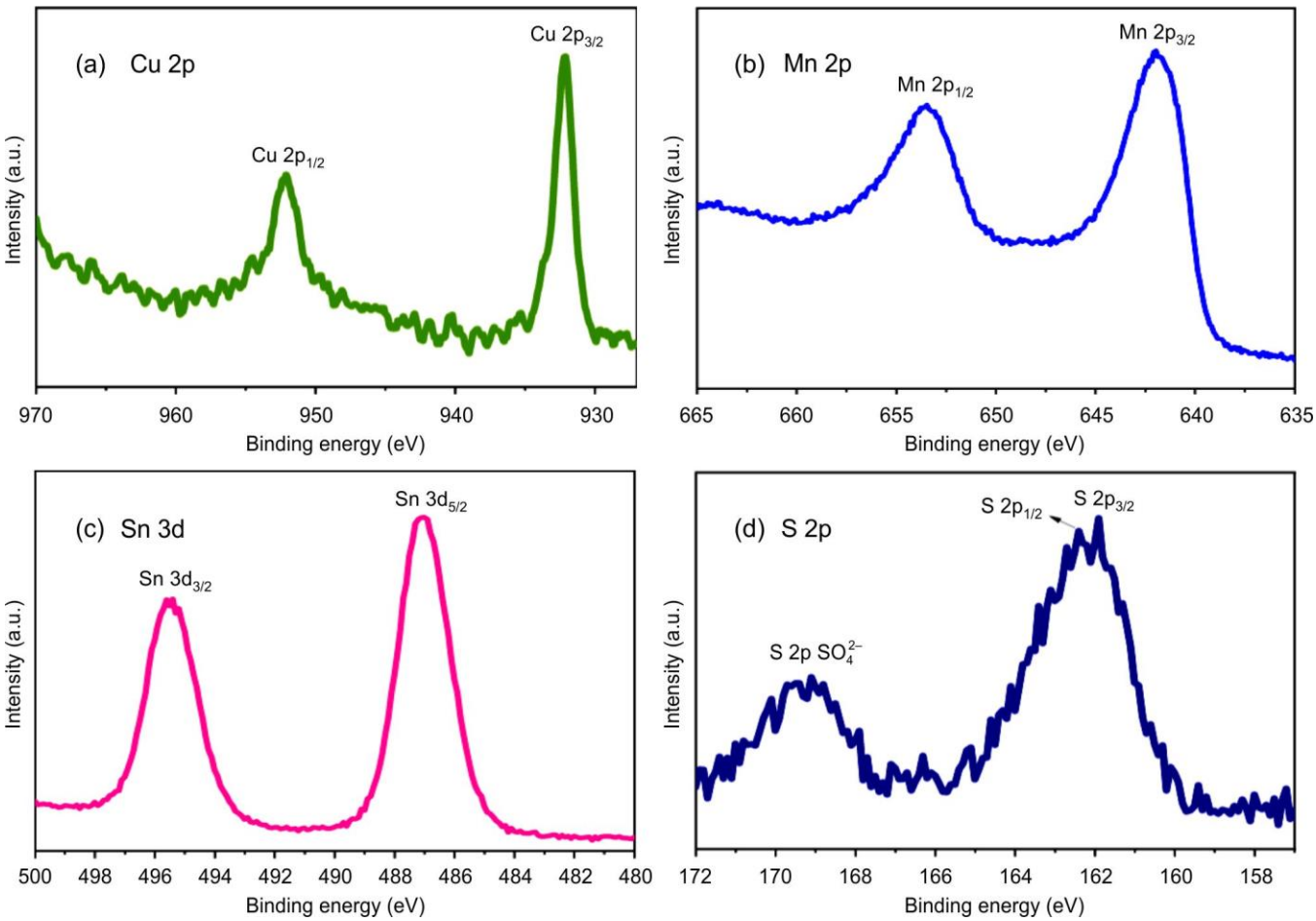

Fig. 5. XPS spectra of $CMTS_{24}$ illustrating (a) Cu, (b) Mn, (c) Sn and (d) S

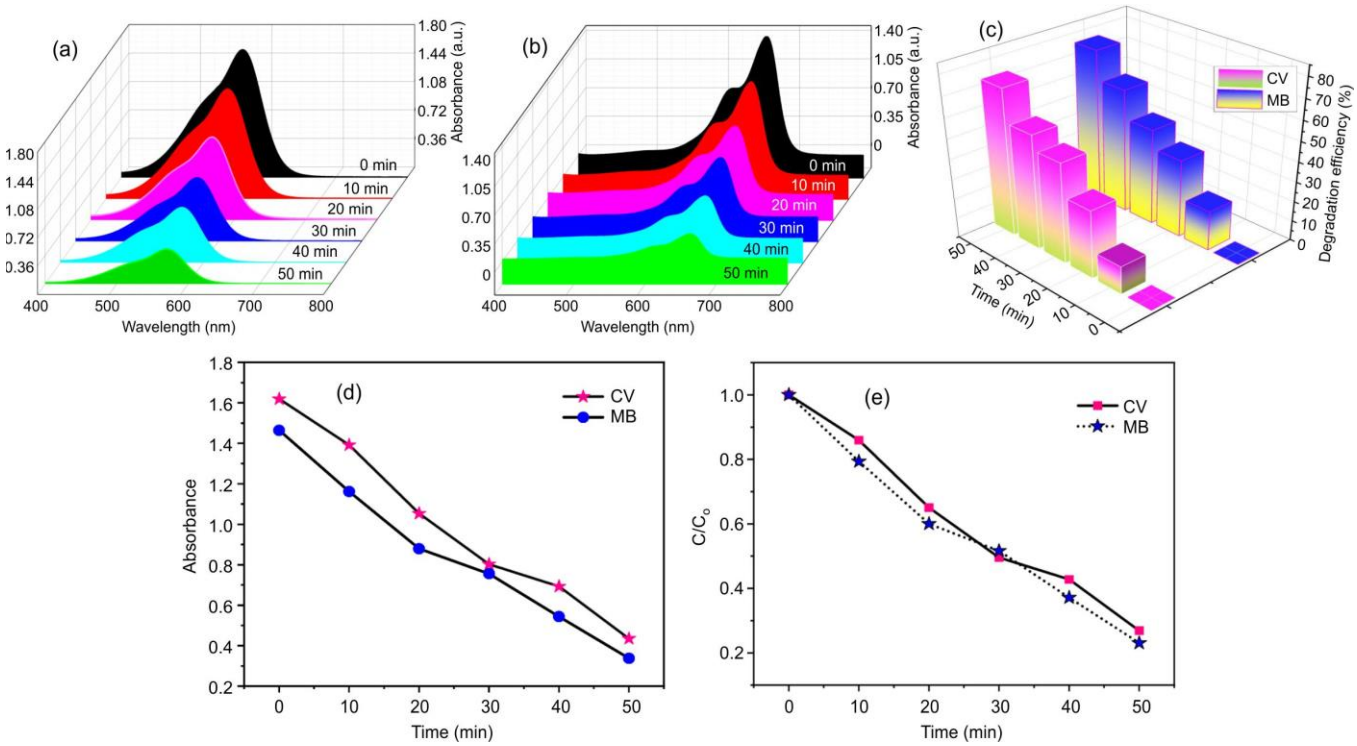

Fig. 6. Photocatalytic degradation performance of $CMTS_{24}$ nanoparticles: (a-b) UV-Vis absorption spectra of MB and CV dyes, (c) degradation efficiency, (d) absorbance *versus* time and (e) C/C_o *versus* time plots showing kinetic behaviour

The $CMTS_{24}$ nanocatalyst, possessing a flower-like hierarchical morphology, demonstrated excellent photocatalytic efficiency, achieving degradation rates of 76% for MB and 73% for CV within 50 min, as quantified using eqn. 1 and illustrated in Fig. 6c. These results affirm the high activity of $CMTS_{24}$ system under solar light exposure. Fig. 6d further emphasizes the temporal reduction in dye concentration, while the C/C_o *versus* time plots in Fig. 6e reveal differing kinetic degradation patterns for MB and CV dyes, attributed to their varied adsorption affinities and redox responses on the catalyst surface. Notably, MB exhibited slightly higher degradation efficiency than CV, potentially due to differences in molecular structure and interaction with active sites on the catalyst surface [12,27].

The superior performance of $CMTS_{24}$ nanomaterial can be linked to its unique nanosheet-assembled flower-like morphology, which offers a high surface area-to-volume ratio, enhanced light-harvesting capability and effective charge carrier separation, all of which contribute to efficient photodegradation [28]. It is widely recognized that the morphological characteristics, crystalline integrity and nanoscale features of a photocatalyst significantly affect its photocatalytic behaviour. These findings suggest that $CMTS_{24}$ nanomaterial is a promising candidate for the solar-driven wastewater treatment technologies.

Photocatalytic degradation mechanism: The proposed mechanism for the sunlight-induced photodegradation of MB and CV dyes using $CMTS_{24}$ nanomaterial as a photocatalyst is illustrated in Fig. 7 and further supported by the reactions outlined in eqns. 4-9 [29-32]. Upon absorbing photons with energy equal to or greater than its bandgap, the CMTS photocatalyst generates electron–hole pairs, as represented in eqn. 4:

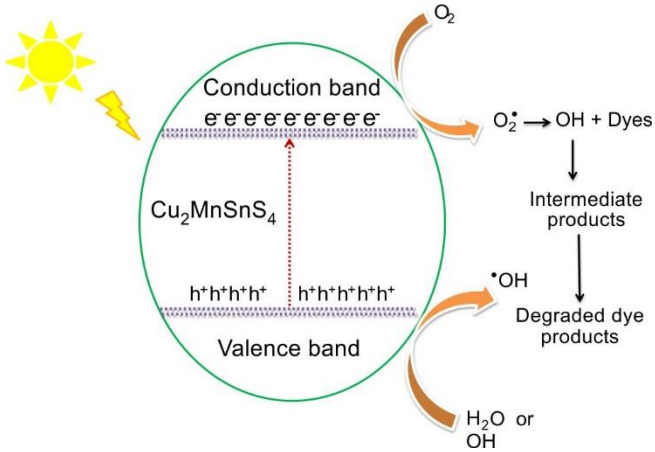

Fig. 7. Schematic of the photocatalytic degradation mechanism of MB and CV dyes using $CMTS_{24}$ sample under sunlight

$$CMTS + h\nu \rightarrow e^- (CB) + h^+ (VB) \quad (4)$$

here, photogenerated electrons in the conduction band (CB) and holes in the valence band (VB) initiate a series of redox reactions. The holes (h^+) oxidize water molecules or hydroxide ions (OH^-), producing hydroxyl radicals ($^{\bullet}OH$), which are highly oxidative species:

$$H_2O/OH^- + h^+ (VB) \rightarrow {}^{\bullet}OH + H^+ \quad (5)$$

Simultaneously, the excited electrons reduce dissolved oxygen molecules (O_2) to form superoxide radicals ($^{\bullet}O_2^-$):

$$O_2 (aq) + e^- (CB) \rightarrow {}^{\bullet}O_2^- \quad (6)$$

These reactive oxygen intermediates undergo further reactions, producing hydrogen peroxide (H_2O_2) and additional hydroxyl radicals:

$$^{\bullet}O_2^- + H^+ \rightarrow HO_2^{\bullet} \rightarrow H_2O_2 \quad (7)$$

$$H_2O_2 + e^- (CB) \rightarrow {}^{\bullet}OH + OH^- \quad (8)$$

Ultimately, these $^{\bullet}OH$ radicals attack and oxidize the dye molecules (MB and CV), leading to their fragmentation into less harmful end products:

$$\text{Dye} + {}^{\bullet}OH \rightarrow \text{Mineralized products} \quad (9)$$

The remarkable photocatalytic activity of $CMTS_{24}$ nanomaterials can be ascribed to its well-engineered flower-like architecture, which facilitates efficient light absorption, rapid charge separation and increased active surface sites for redox reactions. These attributes collectively enhance the generation of reactive oxygen species (ROS), which are crucial for the breakdown of dye pollutants. Thus, $CMTS_{24}$ nanomaterials functions as an efficient, sunlight-responsive photocatalyst for the degradation of organic contaminants, validating its potential application in sustainable and eco-friendly wastewater remediation technologies.

Conclusion

In summary, Cu_2MnSnS_4 (CMTS) nanoparticles with a well-defined flower-like morphology were successfully synthesized *via* a solvothermal approach by varying the reaction duration. XRD and Raman analyses confirmed that extending the synthesis time from 12 h ($CMTS_{12}$ sample) to 24 h ($CMTS_{24}$ sample) led to the formation of a highly crystalline, single-phase kesterite structure with improved purity and structural integrity. The FESEM analysis revealed that $CMTS_{24}$ sample exhibited compact, nanosheet-assembled flower-like architectures, offering a larger surface area and enhanced active site availability. XPS results verified the presence of Cu^+, Mn^{2+}, Sn^{4+} and S^{2-} oxidation states, affirming the correct stoichiometry and chemical composition of the $CMTS_{24}$ sample. The UV-Vis diffuse reflectance spectroscopy indicated strong absorption in the visible range, with a slightly reduced bandgap of 1.66 eV for the $CMTS_{24}$ sample, which is favourable for visible-light driven photocatalysis. The $CMTS_{24}$ nanostructure sample demonstrated remarkable photocatalytic performance by achieving degradation efficiencies of 76% for methylene blue (MB) and 73% for crystal violet (CV) within 50 min under natural sunlight. The improved activity is attributed to the synergistic effect of the optimized morphology, enhanced crystallinity and efficient charge separation. Overall, the findings demonstrated that reaction time is a critical parameter for tuning the structural, morphological and optical properties of CMTS nanomaterials. The $CMTS_{24}$ photocatalyst, with its superior solar-light-driven activity, holds strong potential for practical applications in environmental remediation, particularly for the degradation of organic dye pollutants in wastewater.

ACKNOWLEDGEMENTS

The authors gratefully acknowledge the Head, Department of Physics, and the Centralized Instrumentation and Service Laboratory, Annamalai University, Annamalai Nagar, India, for providing access to the instrumental and analytical facilities supported under DST-FIST and RUSA, which were essential for the successful execution of this research.

CONFLICT OF INTEREST

The authors declare that there is no conflict of interests regarding the publication of this article.

REFERENCES

1. M. Mehta, M. Sharma, K. Pathania, P.K. Jena and I. Bhushan, *Environ. Sci. Pollut. Res. Int.*, **28**, 49434 (2021); https://doi.org/10.1007/s11356-021-15470-5.
2. G.A. El Naeem, A.I. Abd-Elhamid, O.O. Farahat, A.A. El-Bardan, H.M. Soliman and A.A. Nayl, *J. Mater. Res. Technol.*, **19**, 3241 (2022); https://doi.org/10.1016/j.jmrt.2022.06.045
3. O.A. Yildirim, M. Bahadir and E. Pehlivan, *Fresenius Environ. Bull.*, **31**, 9329 (2022).
4. C. Di Iaconi, G. Del Moro, M. De Sanctis and S. Rossetti, *Water Res.*, **44**, 3635 (2010); https://doi.org/10.1016/j.watres.2010.04.017
5. K.H. Hama Aziz, F.S. Mustafa, K.M. Omer, S. Hama, R.F. Hamarawf and K.O. Rahman, *RSC Adv.*, **13**, 17595 (2023); https://doi.org/10.1039/D3RA00723E
6. G. Thennarasu, S. Rajendran, A. Kalairaj, H.S. Rathore, R.C. Panda and T. Senthilvelan, *Clean Technol. Environ. Policy*, **27**, 495 (2025); https://doi.org/10.1007/s10098-024-02960-6
7. R. Ramirez, C. Arellano, J. Varia and S. Martinez, *Curr. Org. Chem.*, **19**, 540 (2015); https://doi.org/10.2174/1385272819061504170947 36
8. S. Dong, J. Feng, M. Fan, Y. Pi, L. Hu, X. Han, M. Liu, J. Sun and J. Sun, *RSC Adv.*, **5**, 14610 (2015); https://doi.org/10.1039/C4RA13734E
9. P. Kush and S. Deka, *ChemNanoMat*, **5**, 373 (2019); https://doi.org/10.1002/cnma.201800321
10. J.H. Malik, M.B. Zaman, R. Poolla, K.A. Malik, I. Assadullah, A.A. Bhat and R. Tomar, *Mater. Sci. Semicond. Process.*, **121**, 105438 (2021); https://doi.org/10.1016/j.mssp.2020.105438
11. A. Bouali, O. Kamoun, M. Hajji, I.N. Popescu, R. Vidu and N. Turki Kamoun, *Technologies*, **13**, 301 (2025); https://doi.org/10.3390/technologies13070301
12. A. Sarathkumar, S. Nithishkumar, G. Sivakumar and K. Mohanraj, *Mater. Sci. Semicond. Process.*, **196**, 109660 (2025); https://doi.org/10.1016/j.mssp.2025.109660
13. J.B. Raval, S.H. Chaki, S.R. Patel, Y.H. Vaidya, A.J. Khimani, P. Thakor, A.B. Thakkar and M.P. Deshpande, *J. Nanopart. Res.*, **27**, 36 (2025); https://doi.org/10.1007/s11051-025-06237-x
14. S. Walake, S. Rondiya, S. Jadkar and Y.A. Jadhav, *J. Mater. Sci. Mater. Electron.*, **36**, 548 (2025); https://doi.org/10.1007/s10854-025-14566-9
15. M. Priya, S. Udhayan, A. Sarathkumar, E. Radhakrishnan, R. Nalini Suja, P. Vasantharani and G. Sivakumar, *Inorg. Chem. Commun.*, **158**, 111539 (2023); https://doi.org/10.1016/j.inoche.2023.111539
16. J.H. Malik, I. Islam, R. Tomar and S.A. Khandy, *Ceram. Int.*, **50**, 42886 (2024); https://doi.org/10.1016/j.ceramint.2024.08.134
17. V.M. Dzhagan, A.P. Litvinchuk, M. Kruszynska, J. Kolny-Olesiak, M.Y. Valakh and D.R. Zahn, *J. Phys. Chem. C*, **118**, 27554 (2014); https://doi.org/10.1021/jp509035f
18. E. Waluś, M. Manecki, G. Cios and T. Tokarski, *Materials*, **14**, 3457 (2021); https://doi.org/10.3390/ma14133457
19. H. Guan, H. Hou, M. Li and J. Cui, *Mater. Lett.*, **188**, 319 (2017); https://doi.org/10.1016/j.matlet.2016.09.018
20. J. Yu, H. Deng, Q. Zhang, J. Tao, L. Sun, P. Yang and J. Chu, *Mater. Lett.*, **233**, 111 (2018); https://doi.org/10.1016/j.matlet.2018.08.147
21. V. Arun, A. Priyadharsan, S. Sivakumar, R. Ranjith, M. Handayani, Muqoyyanah, G.G. Redhyka, M.A. Wadaan, R. Mythili and Y.D. Rahmayanti, *Luminescence*, **39**, e70053 (2024); https://doi.org/10.1002/bio.70053

22. M. Selvam, S. Anbuselvan, N.K. Srinivasan, M. Kannusamy, H.O. Soonmin and S. Ganesan, *Curr. Appl. Sci. Technol.*, **16**, e0260708 (2024); https://doi.org/10.55003/cast.2023.260708
23. N. Karikalan, R. Karthik, S.M. Chen, C. Karuppiah and A. Elangovan, *Sci. Rep.*, **7**, 2494 (2017); https://doi.org/10.1038/s41598-017-02479-5
24. K. Shim, H.W. Kim, S. Park, K.D. Seo, C.Y. Kim, J.B. Lee, J.S. Bae and H.J.A. Kim, *Mater. Adv.*, **5**, 3014 (2024); https://doi.org/10.1039/D4MA00066H
25. F. Butrichi, V. Trifiletti, G. Tseberlidis, B.E. Colombo, F. Taglietti, M. Rancan, L. Armelao and S. Binetti, *Sol. Energy Mater. Sol. Cells*, **272**, 112924 (2024); https://doi.org/10.1016/j.solmat.2024.112924
26. S. Sultana, A. Hore, K. Shams, T. Ur Rashid, M.M. Rahman and M. Shahruzzaman, *Water Pract. Technol.*, **20**, 190 (2025); https://doi.org/10.2166/wpt.2025.006
27. K. Shi, G. Qian, W. Yi, W. Tang, F. Liu, Y. Li, C. Yang, Y. Xiang and H. Yao, *J. Environ. Chem. Eng.*, **12**, 111737 (2024); https://doi.org/10.1016/j.jece.2023.111737
28. P. Sivakumar, C.J. Raj, A.D. Savariraj, R. Manikandan and H. Jung, *Surf. Interfaces*, **51**, 104641 (2024); https://doi.org/10.1016/j.surfin.2024.104641
29. H. Tanaya Das, S. Dutta, K. Gaurav, A. Kanti Giri, A. Mondal, R. Kumar Jena and N. Das, *Chem. Asian J.*, **19**, e202300813 (2024); https://doi.org/10.1002/asia.202300813
30. H. Guan, H. Shen and A. Raza, *Catal. Lett.*, **147**, 1844 (2017); https://doi.org/10.1007/s10562-017-2094-5
31. M.F. Sanakousar, V. C.C, V.M. Jiménez-Pérez, B.K. Jayanna, Mounesh, A.H. Shridhar and K. Prakash, *J. Hazard. Materials Adv.*, **2**, 100004 (2021); https://doi.org/10.1016/j.hazadv.2021.100004
32. O.P. Kumar, M.N. Ashiq, M. Ahmad, S. Anjum and A.U. Rehman, *J. Mater. Sci. Mater. Electron.*, **31**, 21082 (2020); https://doi.org/10.1007/s10854-020-04620-z